Testing some implementations of a cohesive-zone model at finite strain

Pierre Gilormini*, Julie Diani

Laboratoire PIMM, CNRS, Arts et Métiers ParisTech, 151 bd de l'Hôpital, 75013 Paris, France

Abstract

This study shows how the results given by a cohesive-zone model at finite strain may depend strongly on its numerical implementation. A two-dimensional four-node cohesive element is considered, which includes several variants depending on a part of the strain-displacement matrix, on the quadrature rule applied, and on the configuration chosen to perform integration. Finite element simulations combine these variants with a very simple, bilinear, cohesive-zone model, in two tests. The first test involves a single element and illustrates some features of the various implementations. The other test simulates the peeling of an elastomer strip from a rigid substrate.

Keywords: Cohesive-zone model, Cohesive element, Peel test, Finite element analysis

1. Introduction

Cohesive-zone models (CZM) have been used extensively in the last two decades for the finite element simulation of crack propagation or interface debonding. An abundant literature has been published, covering applications in several fields of the mechanics of deformable solids, including fragmentation of brittle solids, delamination in layered composites, particle-matrix debonding, and fracture of adhesive joints. In these models, local fracture occurs gradually in a process zone at the crack tip, where damage develops and stresses keep finite. Barenblatt [1]-[2] introduced this concept very early to include cohesive forces in the context of crack propagation

*Corresponding author. Tel. : + 33 1 44246337; fax: + 33 1 44246190

Email addresses: pierre.gilormini@ensam.eu (Pierre Gilormini*), julie.diani@ensam.eu (Julie Diani)

Published in Engineering Fracture Mechanics, vol. 148, pp. 97-109 (2015).

in elastic solids, and thus avoided stress singularities in brittle fracture. The idea was simultaneously extended to elastic-plastic media by Dugdale [3]. Since these pionering works, many cohesive-zone models have been developed on physical or phenomenological grounds for diverse applications. These models involved a large variety of force-displacement relationships including cubic, exponential, trapezoidal, linear or bilinear softenings, as reviewed for instance by Park and Paulino [4].

The development and practical applications of cohesive-zone models have been closely related to the rapidly growing power of finite element analysis, since analytical solutions are very limited [5]. Needleman [6]-[7], Tvergaard [8], Tvergaard and Hutchinson [9], Xu and Needleman [10] were among the first to implement cohesive-zone models in finite element codes, for inclusion or fibre debonding and for crack growth. Since then, special efforts have been devoted to various numerical aspects of cohesive-zone models regarding in particular the stiffness involved, the fine mesh required, and convergence issues. Among numerous studies, the effect of the numerical integration rule (especially in the context of extremely stiff cohesive zones before damage onset) has been studied by Schellekens and de Borst [11], the connection between the material parameters of the cohesive zone and mesh refinement has been analyzed by Alfano and Crisfield [12], whereas de Borst and coworkers [13]-[14] focused on the bias induced by the initial mesh design in crack propagation. Practical rules have also been proposed by Turon et al. [15] and by Harper and Hallett [16], among others, about the minimum number of elements to be considered in the process zone. The present work also considers numerical aspects of cohesive-zone models, by focusing on various choices that can be made in the implementation and the variety of results that are induced.

This paper is organized as follows. First, the two-dimensional four-node cohesive element considered is described, which includes several variants depending on a part of the strain-displacement matrix, on the quadrature rule applied, and on the configuration chosen to perform integration. The general weak formulation of [17] is used here, and is not repeated for brevity. Then, the simple bilinear cohesive-zone model used is recalled, with emphasis put on some of its properties that are closely related to the cohesive element variants. A first, very simple, test follows, where the cohesive-zone model is combined with these variants, and this enlightens some of their features. Finally, application to the peel test is described, which illustrates the variety of results that can be obtained from a single cohesive-zone model when various choices are made in its numerical implementation. The paper by Paggi and Reinoso [18] (with a recent extension to three-dimensional el-

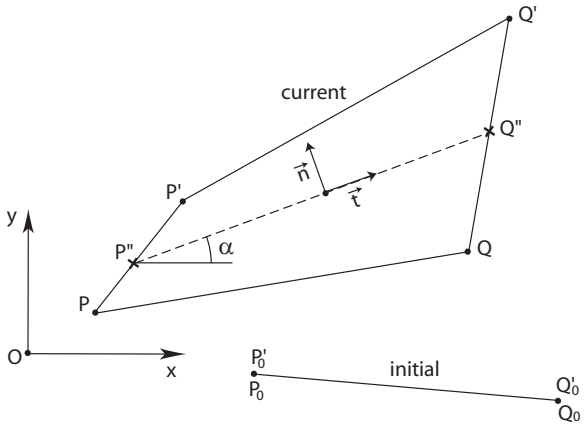

Figure 1: Initial and current configurations of a two-dimensional linear cohesive element illustrating the definition of the local basis vectors by using the middle segment (dashed).

ements [19]) is complementary, it has an analogous organization and follows similar, though not identical, theoretical developments, but with different implementations considered.

2. The cohesive elements considered

The four-node elements considered in this paper are suitable for the two-dimensional plane strain problems studied. The formulation of Ortiz and Pandolfi [20] is applied, which is relevant for large deformations and which introduced the element middle surface. The latter concept, which puts the two sides of the interface on the same footing in the formulation, is illustrated in Figure 1. The linear cohesive element consists initially of a straight segment, where the two sides P_0Q_0 and $P_0'Q_0'$ of the interface coincide, which separate into PQ and $P'Q'$ in the current configuration, and the middle segment $P''Q''$ is defined by the midpoints of the lateral sides PP' and QQ'. Clearly, the orientation of the middle segment with respect to the Cartesian axes is given by the angle

$$\alpha = \tan^{-1}\left[\frac{Q_0^y - P_0^y + (u_y(Q_0) - u_y(P_0) + u_y(Q_0') - u_y(P_0'))/2}{Q_0^x - P_0^x + (u_x(Q_0) - u_x(P_0) + u_x(Q_0') - u_x(P_0'))/2}\right] \qquad (1)$$

where u_x and u_y denote displacement components, P_0^x, P_0^y, Q_0^x, Q_0^y the Cartesian coordinates of P_0 and Q_0, and thus the local element basis $(\overrightarrow{t}, \overrightarrow{n})$

yields, with

$$t_x = C \qquad t_y = S \qquad n_x = -S \qquad n_y = C \tag{2}$$

where $C = \cos\alpha$ and $S = \sin\alpha$. The relative displacement $\overrightarrow{\delta}$ of any point of the P_0Q_0 segment is interpolated linearly between $\overrightarrow{\delta}(P_0) = \overrightarrow{PP'}$ and $\overrightarrow{\delta}(Q_0) = \overrightarrow{QQ'}$, and therefore its local components δ_t and δ_n can be defined from

$$\delta_t(P_0) = (\overrightarrow{u}(P_0') - \overrightarrow{u}(P_0)).\overrightarrow{t} \quad \text{and} \quad \delta_n(P_0) = (\overrightarrow{u}(P_0') - \overrightarrow{u}(P_0)).\overrightarrow{n} \tag{3}$$

with similar expressions for Q_0. The matrix notation used in the numerical implementation of the above equations involves a nodal displacement vector

$$[u]^T = [u_x(P_0)\ \ u_y(P_0)\ \ u_x(Q_0)\ \ u_y(Q_0)\ \ u_x(Q_0')\ \ u_y(Q_0')\ \ u_x(P_0')\ \ u_y(P_0')] \tag{4}$$

where superscript T denotes transposition, the 8×8 orientation matrix $[\tilde{R}]$ where the only nonzero components belong to 4 identical $[R]$ blocks along the diagonal, with

$$[R] = \begin{bmatrix} C & S \\ -S & C \end{bmatrix}, \tag{5}$$

the $[L]$ operator matrix

$$[L] = \begin{bmatrix} -1 & 0 & 0 & 0 & 0 & 0 & 1 & 0 \\ 0 & -1 & 0 & 0 & 0 & 0 & 0 & 1 \\ 0 & 0 & -1 & 0 & 1 & 0 & 0 & 0 \\ 0 & 0 & 0 & -1 & 0 & 1 & 0 & 0 \end{bmatrix}, \tag{6}$$

and the shape-function matrix $[N]$

$$[N] = \begin{bmatrix} N_1 & 0 & N_2 & 0 \\ 0 & N_1 & 0 & N_2 \end{bmatrix}, \tag{7}$$

where the values of N_1 and N_2, between 0 and 1, reflect the linear interpolation at the point considered and need not be more detailed here. As a consequence, the vector of the components of the relative displacement on the local element basis writes

$$[\delta] = \begin{bmatrix} \delta_t \\ \delta_n \end{bmatrix} = [N][L][\tilde{R}][u]\,. \tag{8}$$

The numerical implementation of the element also requires the relative displacement vs. nodal displacement matrix $[B]$, which can be deduced

from the partial derivatives of $[\delta]$ with respect to the nodal displacements $[u]$, $B_{ij} = \partial\delta_i/\partial u_j$. This leads to

$$[B] = [N][L][\tilde{R}] + [N][L][\tilde{R}'][u][A] \tag{9}$$

since matrix $[\tilde{R}]$ depends on $[u]$ through the angle α (see (1)). In the above expression, $[\tilde{R}']$ is the derivative of $[\tilde{R}]$ with respect to α and the components of $[A]$ are

$$[A] = \frac{1}{2\,l}\begin{bmatrix} S & -C & -S & C & -S & C & S & -C \end{bmatrix} \tag{10}$$

where $l = P''Q''$ denotes the current element length. The $[\tilde{B}] = [N][L][\tilde{R}]$ matrix is now introduced; it is such that $[\delta] = [\tilde{B}][u]$, its components are easily obtained as

$$[\tilde{B}] = \begin{bmatrix} -CN_1 & -SN_1 & -CN_2 & -SN_2 & CN_2 & SN_2 & CN_1 & SN_1 \\ SN_1 & -CN_1 & SN_2 & -CN_2 & -SN_2 & CN_2 & -SN_1 & CN_1 \end{bmatrix} \tag{11}$$

and were already given by Park and Paulino [17]. It may be noted that the derivative of the first line of $[\tilde{B}]$ with respect to α is equal to its second line, and the derivative of the second line is equal to minus the first line. Consequently, matrix $[B]$ given in (9) can be rewritten more simply as

$$[B] = [\tilde{B}] + [\tilde{\delta}][A] \qquad \text{where} \qquad [\tilde{\delta}] = \begin{bmatrix} \delta_n \\ -\delta_t \end{bmatrix}. \tag{12}$$

The second term in the right-hand side of the above expression, which conveys that the element basis is not fixed but mobile, was omitted by Park and Paulino [17]. It combines four quantities (products of δ_n and δ_t by C/l and S/l), whereas only two appear in the expression (30) given by Reinoso and Paggi [18]. In practice, this term can be neglected in the case of infinitesimal deformations, since the initially nonzero value of the $[A]$ matrix is multiplied by small δ_t and δ_n components.

The last term in (12) can also be neglected at finite strain in two noteworthy cases. This is due to the $[B]$ matrix being used actually to compute the nodal forces as

$$[f] = \frac{l_i}{2}[B(I_1)]^T[T(I_1)] + \frac{l_i}{2}[B(I_2)]^T[T(I_2)] \tag{13}$$

when two equal-weight integration points I_1 and I_2 are used in the element, as is the case in this work. In the above expression, $[T(I_1)]$ and $[T(I_2)]$ denote the traction vectors (in the local element basis) given by the cohesive-zone

model (as defined in the next section) from the relative displacements at I_1 and I_2. As a consequence of (13), the second term in the right-hand side of (12) contributes to the nodal forces by the $[A]^T$ matrix multiplied by the scalar product $[\tilde{\delta}]^T[T] = \delta_n T_t - \delta_t T_n$. Therefore, this term is zero if the tractions and the relative displacements are colinear, which may apply to some cohesive-zone models. For instance, this is the case in Figure 6 of Reinoso and Paggi [18], who merely noticed "minimal discrepancy" between small and large displacement formulations, because this colinearity is assumed. When such special relation does not apply, the $[A]$ term in (12) can still be neglected in the case of large relative displacements that keep the two sides of the interface (PQ and $P'Q'$) parallel, even if their areas vary. This is due to both the S and C contributions of the $[A]$ matrix to the work of nodal forces being nullified by the resulting combinations of displacement components.

It is worth noticing also that both terms of (12) are required in general to ensure that an incremental rigid body rotation applied to a preliminarily deformed cohesive element does result in a zero increment of external work. For a rotation $\mathrm{d}\alpha$ about the origin of Cartesian axes, obtained through incremental nodal displacements $[\mathrm{d}u]$, the first term leads to $[\tilde{B}][\mathrm{d}u] = -\mathrm{d}\alpha\,[\tilde{\delta}]$ and the second one to $[\tilde{\delta}][A][\mathrm{d}u] = \mathrm{d}\alpha\,[\tilde{\delta}]$; therefore $[B][\mathrm{d}u] = [0]$, leading to $\mathrm{d}W = [f]^T[\mathrm{d}u] = 0$ whatever the traction $[T]$. In the special case where $[T]$ is colinear with $[\delta]$, $\mathrm{d}W$ is still zero if $[A]$ is omitted, because $[T]^T[\tilde{B}][\mathrm{d}u] = -\mathrm{d}\alpha\,[T]^T[\tilde{\delta}] = 0$.

There are two possibilities for the length l_i used in (13), according to integration being performed on either the initial or the current configuration. In the former case, which is considered by Needleman [6]-[7], Tvergaard [8], Ortiz and Pandolfi [20], among many authors who use nominal tractions, $l_i = P_0Q_0$. In contrast, $l_i = P''Q''$ if integration is performed on the current configuration, like in the work of Park and Paulino [17] or Spring and Paulino [21]. This again makes a negligible difference if deformations are infinitesimal, but not at finite strain, as shown below. Two integration schemes are considered in this work: either the Newton-Cotes scheme, which corresponds to taking P'' and Q'' as the positions of I_1 and I_2 in the current configuration (or P_0 and Q_0 in the initial configuration), and the Gauss scheme, where I_1 and I_2 are located on the middle segment $P''Q''$ (or P_0Q_0) at a fraction $(1 - 1/\sqrt{3})/2$ of its length, from each end. Thus, N_1 and N_2 in (7) take the values of 1 and 0, respectively, at point I_1 (and the opposite at I_2) in the Newton-Cotes scheme, whereas values of 0.211 and 0.789 apply to the Gauss scheme. Finally, the $[B]$ matrix is also used to compute the tangent matrix, which is central in the iterative procedure to

solve the problem incrementally but needs not be detailed here (see [17], for instance).

In what follows, the reference cohesive element will be a 4-node linear element using Gauss integration performed on the initial configuration, where the $[B]$ matrix is computed as in (12). This will be referred to as case C1. Three variants will be studied: (i) using the Newton-Cotes scheme (case C2), (ii) performing Gauss integration over the current configuration (case C3), and (iii) additionally neglecting the last term in (12) (case C4). Moreover, the 4-node linear cohesive element (COH2D4) provided by Abaqus will also be used in the comparisons (case C5).

3. The cohesive-zone model considered

Since the aim of this study is to analyze the effects of variations in the numerical implementation of a cohesive-zone model, a very simple one is sufficient. Namely, a special case of the model of Tvergaard and Hutchinson [9] is applied, where a bilinear law (no plateau) is used. One reason for this choice is that 4 material parameters only are required, and another is the availability of this cohesive-zone model in the Abaqus code. Only the essential relations need be recalled here, in order to specify our notations. A state variable λ_m is defined at any interface point, which is the largest value between 0 and 1 reached by the following scalar quantity:

$$\lambda = \sqrt{\left(\frac{\delta_t}{\delta_t^f}\right)^2 + \left(\frac{\delta_n}{\delta_n^f}\right)^2} \tag{14}$$

where δ_t^f and δ_n^f are the relative displacements for interface failure in pure shear ($\delta_n = 0$) and pure normal separation ($\delta_t = 0$), respectively. As long as λ_m is smaller than a critical value λ_c, the interface has an elastic behaviour defined by a tangent stiffness (K_t) and a normal stiffness (K_n), which are assumed to obey the following relation:

$$K_t/K_n = (\delta_n^f/\delta_t^f)^2 \,. \tag{15}$$

Beyond λ_c, the interface damages and the traction vector is given by

$$T_n = (1-D)K_n\,\delta_n \qquad \text{and} \qquad T_t = (1-D)K_t\,\delta_t \tag{16}$$

where the damage variable D is defined as

$$D = \frac{1}{\lambda_m}\frac{\lambda_m - \lambda_c}{1-\lambda_c} \tag{17}$$

and local interface failure ($D = 1$) occurs when $\lambda_m = 1$, which generalizes the special cases of pure shear and pure normal separation mentioned above. Hence, an elastic response is obtained if $\lambda < \lambda_m$ (i.e., unloading or partial reloading), with K_t and K_n stiffnesses if $D = 0$ ($0 \leq \lambda_m \leq \lambda_c$), with $(1 - D)K_t$ and $(1 - D)K_n$ stiffnesses if $0 < D < 1$ ($\lambda_c < \lambda_m < 1$), and with zero stiffnesses if $D = 1$ ($\lambda_m = 1$). Note that the above expressions exclude $\delta_n < 0$, which would correspond to one side of the interface going through the other. One way to avoid such unwanted anomaly is to prescribe a very large normal stiffness if δ_n happens to be negative (and $\delta_n = 0$ must be used formally in the above equations). Another method, which is applied in this study where one side of the interface is a rigid body, takes advantage of the contact algorithms implemented in the finite element code, by prescribing a no-penetration condition.

When $K_t = K_n$, the model of Camanho et al. [22] is recovered if equal energy release rates are assumed for total decohesion in pure shear and pure normal separation. In these conditions, the traction vector is colinear with the relative displacement according to (16), and therefore the $[A]$ matrix can be neglected in the element formulation, as mentioned in Section 2. This explains why the tangent stiffness has been chosen different from the normal stiffness in our numerical applications, since we want to test the effect of neglecting the $[A]$ term in (12). It may also be noted that $K_t = K_n$ corresponds to a simple model in which the two sides of the interface are connected by damageable elastic strings where stretch only matters. This may be a simplified model for polymer fibrils, and in the case of adhesion on a rigid substrate, the number of fibrils per unit substrate surface would play a prominent role, with integration over the initial configuration being appropriate naturally.

This study uses the following four material parameters to apply the cohesive-zone model: the initial normal (K_n) and tangent (K_t) stiffnesses, the critical traction value (T_n^c) for damage initiation in pure normal separation, and the work of separation per unit area of interface (Γ). One reason for choosing this specific set of constants is an easy application of the Abaqus user interface, and the other parameters used above are then given by $\delta_n^f = 2\Gamma/T_n^c$, $\delta_t^f = \delta_n^f\sqrt{K_n/K_t}$, and $\lambda_c = 2\Gamma/(K_n(\delta_n^f)^2)$. The following values are used in the numerical applications: $K_n = 20$ GPa/m, $K_t = 5$ GPa/m, $T_n^c = 0.02$ MPa, $\Gamma = 1$ J/m^2. The latter value is representative of the adhesion of an elastomer, and consequently the T_n^c value is associated with $\delta_n^f = 100$ μm, which is typical of fibrils length at rupture in elastomers. The stiffness ratio follows from the analysis of Geymonat et al. [23] for an interface made of an isotropic elastic layer with a thickness

tending to zero, namely $K_n/K_t = 2(1+\nu_l)/(1-2\nu_l)$, and a layer Poisson's ratio ν_l equal to 0.2 has been used here to keep the stiffness ratio within reasonable and illustrative limits.

It can be checked easily that the traction components (16) when damage increases ($\lambda_m = \lambda$ between λ_c and 1) are the partial derivatives of the following potential

$$\phi(\lambda) = \Gamma - \frac{K_n(\delta_n^f)^2}{2}\frac{\lambda_c}{1-\lambda_c}(1-\lambda)^2 \tag{18}$$

with respect to δ_t and δ_n, respectively, provided that condition (15) is satisfied. Therefore, one has $\phi = (T_n^c)^2/(2K_n)$ at damage onset and $\phi = \Gamma$ at rupture for any combination of tangent and normal relative displacements. This independence with respect to mode mixity is a feature of the Tvergaard and Hutchinson [9] model that will be very useful in the simulation of the peel test in Section 5. Since the only source of energy dissipation here is the damage process, the energy dissipated along a length $\mathrm{d}l_i$ of interface, per unit out-of-plane thickness, is given by the difference between the current value of the potential minus the elastic energy stored, times $\mathrm{d}l_i$, i.e.,

$$\mathrm{d}W_D = \left(\phi - \frac{1}{2}\overrightarrow{T}.\overrightarrow{\delta}\right)\mathrm{d}l_i = \frac{\lambda-\lambda_c}{1-\lambda_c}\,\Gamma\,\mathrm{d}l_i \tag{19}$$

when (18), (16) and (17) are used with $\lambda_m = \lambda$. Therefore, if $\mathrm{d}l_i$ keeps equal to the initial length of the interface segment considered, the energy dissipated at fracture ($\lambda = 1$) will be equal to Γ times this initial length. In other words, the work to separate an interface is known in advance, before the loading has started, by knowing the adhered area and Γ. In contrast, if $\mathrm{d}l_i$ denotes the current length of the interface segment, which may vary for instance when one side rotates with respect to the other as shown in Section 4, the energy required for complete separation is hardly predictable. This stresses a consequence of the configuration, either initial or current, chosen when implementing the cohesive element. Another consequence may be a more complex experimental procedure required to identify the parameters of a cohesive-zone model.

The equations defining both the cohesive element described in Section 2 and the cohesive-zone model detailed here have been implemented as a user element routine in the Abaqus [24] code. The Fortran program given by Park and Paulino [17] at the end of their paper, where a much more complex cohesive-zone model was considered [25], has been very helpful in this process. The latter program did not include the $[A]$ term of (12) and used

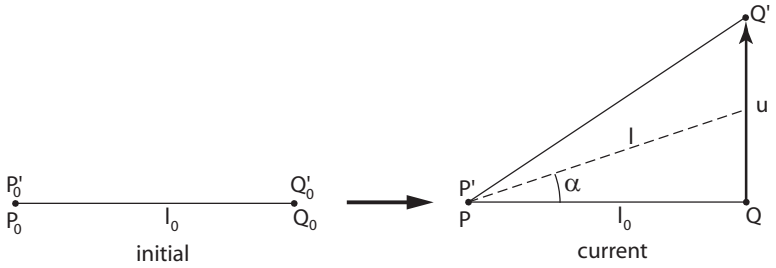

Figure 2: The wedge test, as applied to a single cohesive element.

the current configuration for Gaussian quadrature, but only a few lines had to be added or modified to modify these points. This cohesive user element will allow an easy comparison of the implementation variants listed at the end of Section 2. It will also allow to mimic the COH2D4 cohesive element of Abaqus in order to analyze its implementation.

4. The wedge test

All the considered variants of the cohesive user element, as well as the Abaqus cohesive element, do give expected results when a single element is considered and one side of the interface is translated with respect to the other: the history of each traction component follows a triangular profile, for any mode mixity, when the δ_t/δ_n ratio keeps constant. Moreover, the dissipated energy at rupture ($D = 1$) equals Γ times the initial (constant) element length per unit out-of-plane thickness, for any displacement history, even if the δ_t/δ_n ratio is not constant, i.e., for non proportional loadings. Clearly, such loadings allow to check basic requirements of the implementation of the cohesive-zone model, but they are not able to test its results at finite strain, which requires to develop a significant angle between the two sides of the interface. This is the purpose of the test applied in this section, where a cohesive element with an initial zero thickness and a unit out-of-plane thickness is transformed into a right triangle by moving a single node, as shown in Figure 2. Thus, the interface opens widely to become wedge-shaped. If the mobile node moves by a length u, (1) gives the simple result $\alpha = \tan^{-1}(u/2l_0)$, where l_0 denotes the initial element length, and thus

$$\frac{\mathrm{d}\alpha}{\mathrm{d}u} = \frac{l_0}{2(l_0^2 + u^2/4)} \tag{20}$$

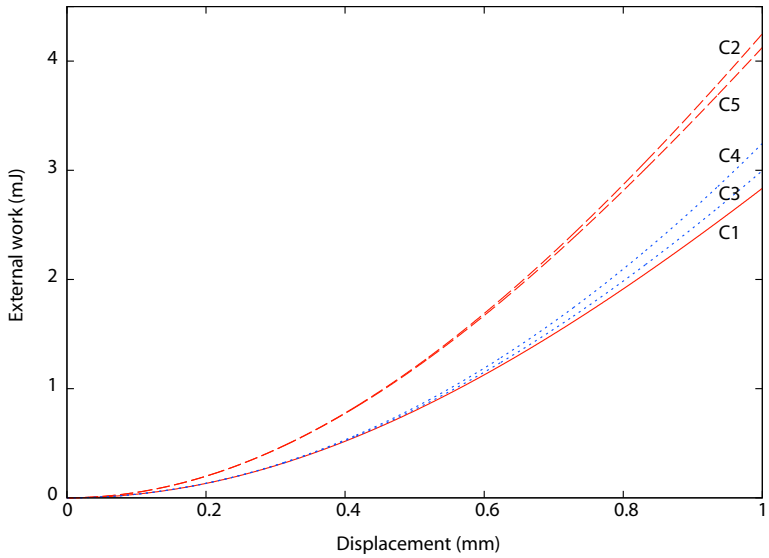

Figure 3: External work computed in the wedge test applied to an elastic cohesive zone with 1 mm width and 1 mm out-of-plane thickness. Computations with a single cohesive user element applying Gauss integration (over initial configuration: unbroken curve C1, or over current configuration: lower dotted curve C3) with $[A]$ term included, or neglected (upper dotted curve C4, with Gauss integration over current configuration), or applying Newton-Cotes integration over initial configuration (upper dashed curve C2). Lower dashed curve C5 corresponds to using a single Abaqus cohesive element. Red and blue curves pertain to integrations over initial and current configurations, respectively.

decreases from 0.5 to 0.4 when u increases from 0 to l_0, for instance. This is what the $[A]$ matrix of Section 2 reduces to in the present case. Simultaneously, the element length, as defined in Section 2, is given by

$$l = \sqrt{l_0^2 + u^2/4} \tag{21}$$

and increases by 12% in the above conditions.

Consider first a purely elastic cohesive zone, i.e., with K_t and K_n as only parameters. The increment of external work per unit out-of-plane thickness induced by an increment of displacement $\mathrm{d}u$ can be computed exactly from

$$\mathrm{d}W = \frac{u\, l_i}{3}\left[K_t \sin^2\alpha + K_n \cos^2\alpha + (K_t - K_n)\frac{\mathrm{d}\alpha}{\mathrm{d}u}\sin\alpha\cos\alpha\right]\mathrm{d}u = F\ \mathrm{d}u \tag{22}$$

where the integration of $\overrightarrow{T}.\,\mathrm{d}\overrightarrow{\delta}$ has been performed along the length l_i, and where F denotes the force applied at the moving end of the interface. This

expression shows that the effect of $\mathrm{d}\alpha/\mathrm{d}u$ is nullified if $K_t = K_n$, as expected from Section 2. This expression also shows that taking $l_i = l$ instead of $l_i = l_0$ multiplies merely the nodal force by $\sqrt{1 + (u/2l_0)^2}$, according to (21), but the resulting increase in external work W is less simple. In contrast, the external work has a closed-form expression if integration is performed on the initial configuration:

$$W = \frac{u^2 l_0}{6} \frac{K_n l_0^2 + K_t u^2/4}{l_0^2 + u^2/4} \tag{23}$$

per unit out-of-plane thickness. This is exactly what is obtained for the unbroken curve C1 in Figure 3, i.e., when a single cohesive user element with Gauss integration performed over the initial configuration is used in an Abaqus simulation with very small increments. This happens because the $\overrightarrow{T} . \mathrm{d}\overrightarrow{\delta}$ scalar product evolves quadratically along the element, and therefore Gauss integration provides the exact result. In contrast, Newton-Cotes integration over a single element multiplies the exact result by 3/2 in these conditions, which explains why the upper dashed curve C2 in Figure 3 is 50% higher than C1. The lower dotted line C3 corresponds to Gauss integration performed over the current configuration, i.e., taking $l_i = l$, which induces an increase slightly lower than (21) would predict (recall the effect on the external work is more complex than on the nodal force, as mentioned above, because l varies with u during integration). In addition, the $[A]$ term has been neglected in the cohesive element used to compute the upper dotted curve C4, which leads to an additional increase of external work. This is consistent with the minus sign of the $\mathrm{d}\alpha/\mathrm{d}u$ term in (22) when $K_t < K_n$, as is the case in the numerical application. The lower dashed curve C5 corresponds to using the Abaqus cohesive element COH2D4 in the simulation. We could reproduce this result exactly with the cohesive user element in the following conditions: Newton-Cotes integration performed over the initial configuration, with the $[A]$ term duely taken into account, but using a uniform δ_t value equal to the average between the values taken at the two element ends. The latter point explains a result close, but not equal, to the upper dashed curve C2, and it is consistent with the general observation that uniform tangent strain values are displayed over each COH2D4 element in Abaqus contour maps, whereas other values (normal strain, for instance) are not. The use of Newton-Cotes integration in the COH2D4 element is consistent with the Abaqus documentation, and has the effect that a given integration point pertains to two neighbour cohesive elements, with consequently two values available at the same place, which are different in general. This may be confusing when damage is considered, for instance.

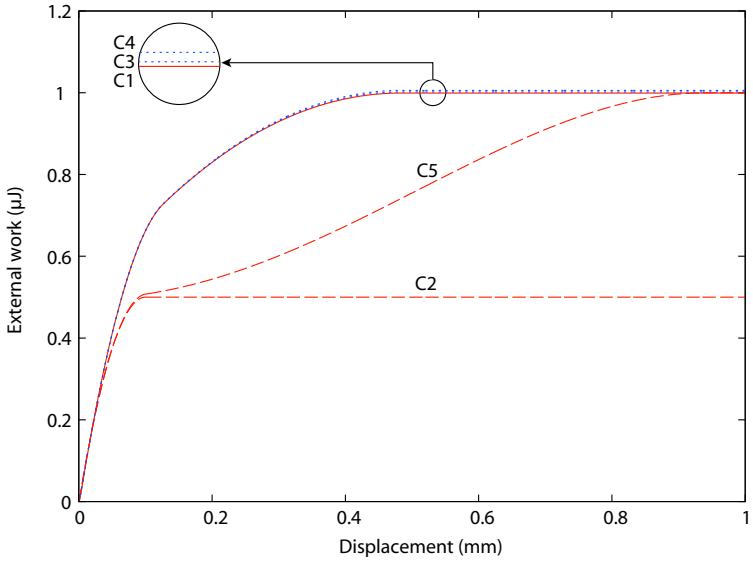

Figure 4: External work computed in the wedge test applied to a damageable cohesive zone with 1 mm width and 1 mm out-of-plane thickness. Computations with a single cohesive user element applying Gauss integration (over initial configuration: unbroken curve C1, or over current configuration: lower dotted curve C3) with $[A]$ term included, or neglected (upper dotted curve C4, with Gauss integration over current configuration), or applying Newton-Cotes integration over initial configuration (lower dashed curve C2). Upper dashed curve C5 corresponds to using a single Abaqus cohesive element. Red and blue curves pertain to integrations over initial and current configurations, respectively.

The more realistic case of the damageable cohesive-zone model described in Section 3 is considered now, and the corresponding external works computed in the above five cases are shown in Figure 4. The reference case C1 (Gauss integration over initial configuration and $[A]$ term included) does reach a plateau at the level $W = l_0\Gamma$, as expected (unbroken curve), but integrating over the current configuration (lower dotted curve C3) gives now a scarcely higher plateau ($+\,0.2\%$), and similarly ($+\,0.6\%$) when, in addition, the $[A]$ term is neglected (upper dotted curve C4). This is due to a rapidly decreasing nodal force when damage proceeds, which weakens the concomitant and moderate l increase. Since there is no relative displacement at one end of the element, damage cannot develop at this integration point in the Newton-Cotes scheme, and therefore the other integration point only is damaged. This is the reason why the lower dashed curve C2 in Figure 4 rapidly reaches a $l_0\Gamma/2$ plateau. In contrast, the averaging of the δ_t components

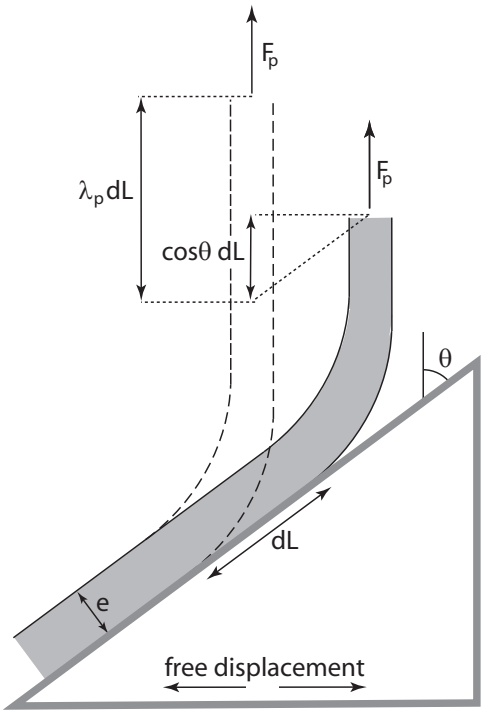

Figure 5: Notations used in the analysis of the peel test. For clarity, the view is linked to the moving substrate and consequently the vertical direction of the applied force translates horizontally. Of course, the opposite occurs in the framework of the testing machine.

in the Abaqus COH2D4 element induces damage at both Newton-Cotes integration points, which explains that finally the upper dashed curve C5 reaches the $l_0\Gamma$ plateau.

The wedge test is very academic, inasmuch as a single cohesive element is involved, but it has allowed to illustrate the effects of two typical features of large deformations, namely the configuration used for integration and the $[A]$ term in (12). The effects are substantial if the cohesive zone remains elastic, but they are weakened significantly when damage develops. The role of the integration scheme also has been analyzed, with consequences that keep significant for a damageable cohesive zone. These simulations have allowed to check all the variants of the cohesive element that have been implemented and to analyze how the Abaqus COH2D4 cohesive element behaves. This is important for being confident in the following simulations of the peel test.

5. The peel test

The peel test is a particularly simple and common technique to measure the adhesion energy between a thin film and a substrate [26]. It consists in peeling a thin strip of material at a constant angle from a substrate that is free to translate, until a steady state is reached, i.e., the peel force F_p reaches a plateau. As shown in Figure 5, peeling a strip length $\mathrm{d}L$ in the steady state induces an increment of external work equal to $F_p(\lambda_p - \cos\theta)\,\mathrm{d}L$, where θ denotes the peel angle and λ_p the stretch ratio of the strip. A hyperelastic elastomer strip is considered here, and therefore the incremental external work is equal to the sum of the stored elastic strain energy $U b\, e\, \mathrm{d}L$, where U denotes the strain energy per unit undeformed strip volume, e the strip thickness and b its width, plus the separation energy $\Gamma_p\, b\, \mathrm{d}L$ dissipated in the peeling process. Therefore, the peeling separation work per unit surface Γ_p, which may depend on such parameters as the peel angle through mode mixity, for instance, can be derived exactly by equating the two evaluations of the incremental external work:

$$\Gamma_p = (\lambda_p - \cos\theta) F_p / b - e\, U \tag{24}$$

as obtained already by Lindley [27], who used this equation to deduce the apparent peeling separation work exactly from the material (U), geometric (θ, b, e), and measured (λ_p, F_p) data involved in the peel test performed on a hyperelastic elastomer. In the special case of small-strain elasticity and assuming the strip is under uniaxial tension, this equation recovers the result obtained by Kendall [28] and, previously but in Japanese, by Hata et al. [29]. For an inextensible strip ($\lambda_p = 1$ and $U = 0$), as applies well to adhesive tapes for instance, the expression derived very early by Rivlin [30] is recovered, which specializes to the simple relation $\Gamma_p = F_p/b$ for a peeling angle of 90°, i.e., the work of adhesion per unit surface is equal to the peeling force per unit strip width. It may be noted that if a cohesive-zone model is used that involves a work of separation Γ independent of mode mixity and referred to the initial configuration, the peeling separation work Γ_p will be equal to Γ. In these conditions, (24) provides an exact analytical relation between material data (Γ and U), process parameters (θ, b, e), and measures (λ_p, F_p), which is rarely the case for problems involving large deformations. When the strip is elastic-plastic [31]-[32] or viscoelastic [33], for instance, the peel test is more complex and no analytical solution is available. Nevertheless, it is worth mentioning that a hyperelastic behaviour may be realistic for the peeling of an elastomer at very low speed, when viscous effects can be neglected and the peel force becomes independent of the peel rate, as in the

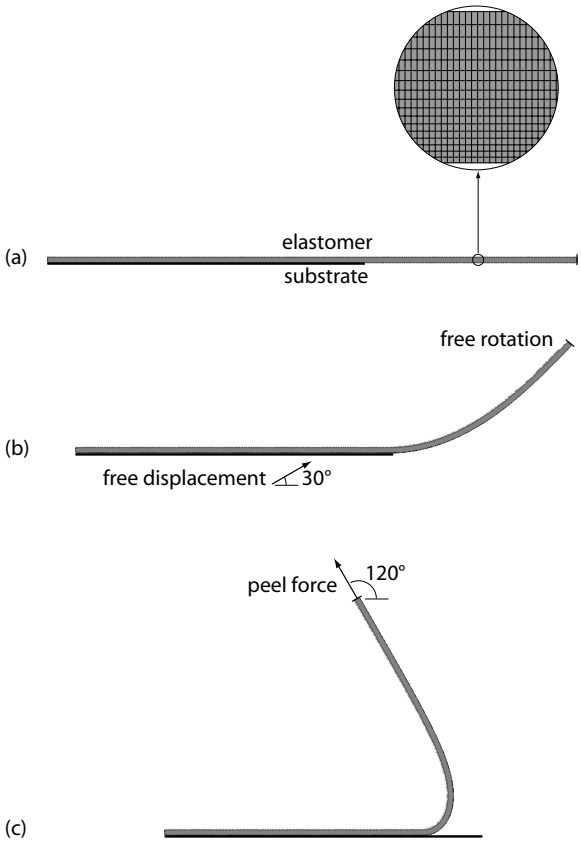

Figure 6: Initial (a), intermediate (b) and final (c) configurations in the finite element simulation of a peel test at 120°. Inset shows an enlarged view of the initially periodic mesh used.

experiments of [26] for example. Of course, the present simulations of the peel test are still oversimplified, since a very simple cohesive-zone model is considered in addition to a hyperelastic elastomer, but they take advantage of an exact analytical solution for a precise evaluation of numerical tests. This analytical solution was not considered by Reinoso and Paggi [18] in their analysis of the peeling of a hyperelastic elastomer with two different cohesive-zone models.

Our finite element simulations of the peel test (see Figure 6) consider an initially straight strip of elastomer, which adheres on a rigid substrate along a fraction of its length, and which deforms in plane strain. The strip length

is 25 mm, including an adhered length of 15 mm, which has been checked to allow reaching a steady peel force with such free strip length and remaining adhered length that strip end effects are negligible (note that the above analytical solution assumes these length are infinite, in principle). The initial structured mesh is periodic along the strip length, with an element length of 10 μm, and the mesh size increases as a geometric sequence from 10 μm to 21.5 μm in 17 layers through the 0.25 mm strip thickness (see Figure 6 inset). The 42,500 elements defining the strip use displacements and pressure as unknown variables (CPE4RH Abaqus hybrid elements with reduced integration), since the elastomer considered is almost incompressible. More precisely, its behaviour is neo-Hookean, which is sufficient for the moderate strains involved, with an elastic energy defined by

$$U = \frac{E}{4(1+\nu)}\left(\frac{1}{J^{2/3}}\mathrm{tr}(\mathbf{F}\mathbf{F}^T) - 3\right) + \frac{E}{6(1-2\nu)}(J-1) \tag{25}$$

where $\mathbf{F}$ denotes the transformation gradient and J its determinant. $E = 1$ MPa and $\nu = 0.495$ are the Young modulus and Poisson's ratio that would apply at small strain. A layer of 1500 identical zero-thickness cohesive elements (10 μm long) connects the elastomer strip to the rigid substrate, where the cohesive-zone model described in Section 3 applies. Suitable boundary conditions are applied to forbid penetration into the substrate and to allow the free translation of the latter in the direction normal to the peel direction. A displacement in the peel direction is applied to the free end of the strip, which moves as a freely rotating rigid body. As illustrated in Figure 6, the strip first bends, the force increases, then the peel angle stabilizes, separation from the substrate begins and the force reaches a plateau. Three key quantities are recorded: the peel force F_p conjugate to the displacement applied to the strip end, the stretch ratio λ_p and the elastic energy per unit volume U at sufficient distance (twelve times the strip thickness) from the strip end in order to neglect end effects. No stabilization viscous scheme was used in the simulations, which would have added an artificial dissipation that could affect the peel force.

Mesh convergence has been checked by testing various mesh sizes along the strip length, and Figure 7 presents the oscillating peel force obtained when using the reference implementation (C1). These oscillations, which keep the peel force with the same average value, are related to an element of the periodic mesh entering or leaving the process zone where separation proceeds, and it can be checked that the period is equal to the length of an element indeed. It can also be observed in Figure 7 that the amplitude of the oscillations is substantially reduced (2.21 %, 0.53 %, 0.02 % of the

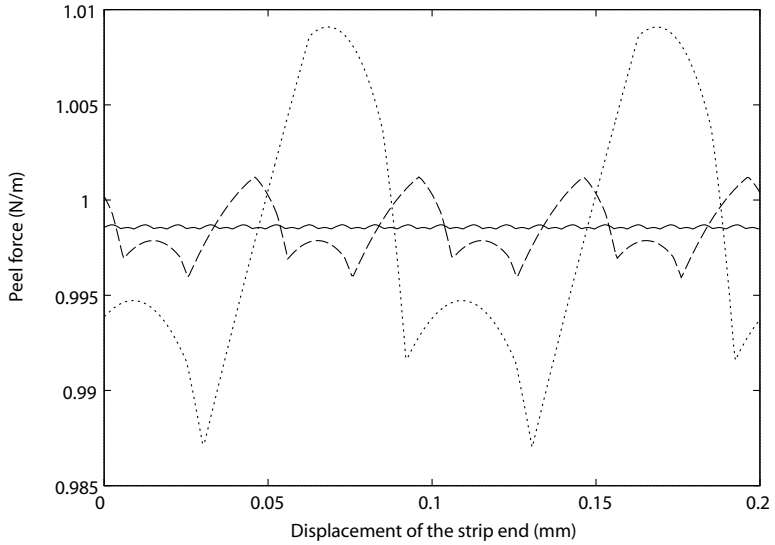

Figure 7: Peel forces per unit out-of-plane thickness obtained with a mesh size of 100 μm (dotted curve), 50 μm (dashed curve), and 10 μm (unbroken curve) along the strip length, using the reference implementation (C1). Peel angle: 90°.

average force value) when the mesh size is finer, and a 10 μm mesh size can be considered as providing a very good approximation of the exact solution. Very similar results were obtained with the other implementations (C2 to C5), with slightly different average values because different implementations may lead to different peel forces. It is worth noting that no fluctuation was found along the process zone of such quantities as stress or damage, whatever the implementation considered. This differs from what Schellekens and de Borst [11] observed and may be due to the specific set of values chosen for the material parameters.

The results obtained by combining the finite element simulations and (24) are reported in Table 1, where the normalized difference $(\Gamma_p - \Gamma)/\Gamma$ is given in percent. This table illustrates the diversity of values that can be obtained with various numerical implementations of a given cohesive-zone model, with fixed material parameters. A large span of peel angles is studied, and the four variants of the cohesive user element already considered in Section 4 are used (cases C1 to C4), as well as the Abaqus COH2D4 cohesive element (case C5). In addition, the surface-based cohesive behaviour also available in Abaqus is considered, where the line of cohesive elements is removed and the cohesive-zone model (with the same parameters) is ap-

Peel angle	30°	60°	90°	120°	150°
Gauss on initial config., $[A]$ included (C1)	0.00	0.00	0.00	0.00	0.00
Newton-Cotes on initial config., $[A]$ included (C2)	−0.02	0.00	0.01	0.00	0.00
Abaqus COH2D4 cohesive element (C5)	0.02	0.01	0.05	0.02	0.00
Gauss on current config., $[A]$ included (C3)	3.57	3.98	4.32	4.56	4.79
Gauss on current config., $[A]$ neglected (C4)	6.84	7.47	8.08	8.56	9.00
Abaqus surface-based cohesive behaviour	8.19	9.33	10.16	10.74	11.31

Table 1: Relative difference, in percent ($100\times(\Gamma_p - \Gamma)/\Gamma$), between the peeling works of adhesion obtained from finite element simulations and the work of separation assumed by the cohesive-zone model, for various peel angles, using different types of cohesive elements or a surface-based cohesive behaviour.

plied directly between the bottom face of the elastomer strip and the rigid substrate. Since this appears as a convenient alternative to using cohesive elements in the peel test, it seemed important to test its effects on the results.

As expected from the mesh convergence analysis and from the mode-mixity independence of Γ, the first line of Table 1 gives $\Gamma_p = \Gamma$ with the excellent precision of less than a hundredth of one percent for all peel angles. Comparison with the second line shows that Newton-Cotes and Gauss quadratures give very similar results in the simulation of the peel test, a fact that may be due to using a very fine mesh and was not expected from the wedge test of Section 4. Moreover, no convergence problem was observed with either quadrature scheme. The Abaqus COH2D4 element (third line of Table 1) also is consistent with the results given by these two variants of the cohesive element, which is interesting because such values as damage can be plotted from the COH2D4 elements, which is not possible with Abaqus when user elements are employed. One drawback of the COH2D4 element is a slower convergence, though, since using the automatic time-stepping procedure of Abaqus required significantly larger numbers of increments, with more iterations, than for the cases in the first two lines of Table 1, resulting in much longer computing times. This may be due to the computation of the stiffness matrix but has not been analyzed further in the present work.

The values reported in the last three lines of Table 1 are significantly larger than in the first three lines, and this is related to their use of the current configuration to integrate the cohesive-zone model. As already mentioned, using the current configuration may lead to unexpected values of the effective work of adhesion, but the results of Section 4 did not anticipate

the rather large values reported in the fourth line of Table 1, where only the configuration used for integration has changed with respect to the first line. Figure 8 illustrates the mode-mixity that takes place in the process zone, where the cohesive elements are both elongated and sheared, but interpreting the variations in the fourth line of Table 1 as an effect of the peel angle on the work of separation per unit surface due to mode mixity would be erroneous, since there is no such influence in the cohesive-zone model used. Figure 8 shows that the length of the process zone decreases when the peel angle increases and, since its height (related to the largest relative displacement at failure) is almost constant, the stretch ratio of the middle surface also increases. This explains the apparent effect of the peel angle in the fourth line of Table 1 by purely geometrical reasons. Based on our convergence study, we emphasize the accuracy of the values in the third line of Table 1 (as well as in the whole table), which do reflect the confounding effect of using the current configuration in the implementation of the cohesive-zone model.

The fifth line of Table 1, i.e., when the implementation choices made in [17] are applied, shows that neglecting the mobility of the local element basis almost doubles the values obtained in the fourth line, where this is accounted for. Therefore, neglecting the $[A]$ matrix is clearly not admissible in these simulations of the peel test. It has been checked with additional simulations that the fourth and fifth lines of Table 1 do become interchangeable if K_t is taken equal to K_n, i.e., when the tractions and relative displacements become colinear, as expected from Section 2.

Finally, the sixth line of Table 1 shows the results obtained when the surface-based cohesive behaviour was used instead of a cohesive element. In order to assess that integration was performed over the current configuration, a single hyperelastic element in contact with a plane rigid surface was considered in a preliminary test. The deformable element has been either elongated or contracted parallel to the interface until complete contact rupture in pure shear mode, and it was then returned to its original shape in order to deduct its strain energy from the external work. Therefore, the latter gave direct access to the energy dissipated by the contact rupture and, using the same cohesive-zone parameters as above, these simple simulations lead to effective adhesion energies 13.5 % larger or smaller than Γ, according to wether the deformable element had been first elongated or contracted. When applied to a cohesive user element with Newton-Cotes quadrature performed on the current configuration (not considered further in this study, for brevity), the same procedure lead to half these values. This is consistent with the Abaqus surface-based cohesive behaviour using the nodes of the

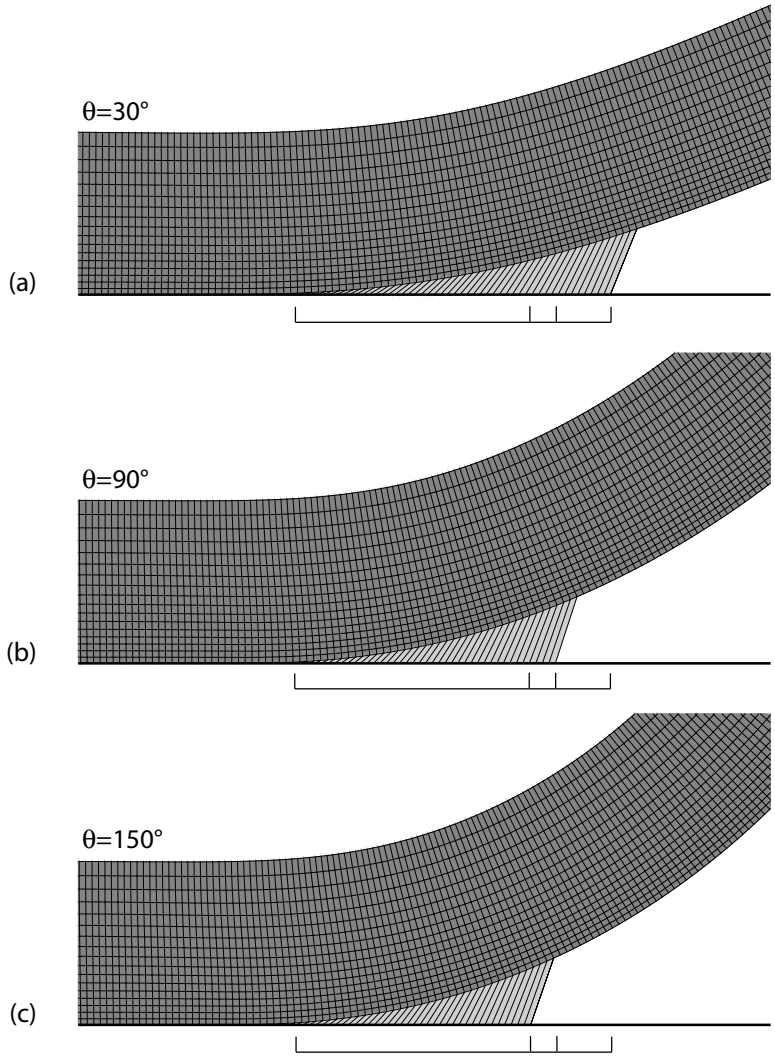

Figure 8: Enlarged views of the deformed strip (dark gray) and of the deformed cohesive elements in the process zone (light gray, where $0 < D < 1$), for peel angles of (a) 30°,(b) 90°, and (c) 150°. These simulations used COH2D4 cohesive elements.

"master" surface to define the local coordinates in an asymmetric formulation based on a master-slave pair, rather than the middle surface used by cohesive elements. This also explains why the last line of Table 1 shows the largest values, and the big differences with the third line initiated our systematic study of the effect of numerical implementations, actually.

6. Conclusions

This study has shown how the results given by a cohesive-zone model at finite strain may depend strongly on some details of its numerical implementation. It is important for the user to be aware of such possibly implicit details if a cohesive-zone model has to be implemented, which would use cohesive elements available in a finite element code, for instance. By using a very simple cohesive-zone model, which is accessible in the Abaqus finite element code, combined with a suitable and versatile user element, this study has demonstrated the following points:

1. Although less precise for the elastic part of the cohesive-zone model, Newton-Cotes integration has given results in very good agreement with Gauss quadrature for the peeling of an elastomer adhered on a rigid substrate. Moreover, both schemes lead to similar convergence and computing times.
2. Neglecting the mobility of the local basis in the element formulation has no consequence when tractions and relative displacements are colinear in the cohesive-zone model, but this may lead to large errors with more general models, especially in the peel test. This is a typical feature that is negligible when deformations keep small.
3. Integrating the cohesive-zone model on the current configuration rather than on the initial configuration may lead to large differences in the work of separation per unit surface involved in the peel test, and this may be confusing about the effect of the peel angle, for instance. The choice of the configuration used for the integration of a cohesive-zone model must be physically justified, and this must be explicitly specified to the user. This is another typical feature of finite strain.
4. The simplest cohesive element available in the Abaqus code, which includes the mobility of the local basis and performs integration on the initial configuration, has given very satisfactory results for the peeling of an elastomer adhered on a rigid substrate, although it averages the tangential components of the relative displacement. One should nevertheless be careful when other applications are considered, as the wedge test presented in this study has shown.

5. The surface-based cohesive behaviour that is also available in the Abaqus code is not equivalent to the cohesive element, since it integrates the cohesive-zone model on the current configuration and does not use the middle surface concept but rather an asymmetric master-slave formulation. It should be used very cautiously when precise results are expected and it is not recommended for the simulation of the peel test.

This approach based on critical tests can be extended to more complex cohesive elements (with nonlinear interpolation or three-dimensional, for instance) and to more elaborate cohesive-zone models, in order not to spoil the complexity of a refined physical theory by an improper numerical implementation in a finite element code.

References

[1] Barenblatt GI. The formation of equilibrium cracks during brittle fracture. General ideas and hypotheses. Axially-symmetric cracks. J Appl Math Mech 1959;23:622-636.

[2] Barenblatt GI. The mathematical theory of equilibrium cracks in brittle fracture. Adv Appl Mech 1962;7:55-129.

[3] Dugdale DS. Yielding of steel sheets containing slits. J Mech Phys Solids 1960;8:100-104.

[4] Park K, Paulino GH. Cohesive zone models: A critical review of traction-separation relationships across fracture surfaces. Appl Mech Rev 2011;64:060802/1-060802/20.

[5] Williams JG, Hadavina H. Analytical solutions for cohesive zone models. J Mech Phys Solids 2002;50:809-825.

[6] Neddleman A. A continuum model for void nucleation by inclusion debonding. J Appl Mech 1987;54:525-531.

[7] Neddleman A. An analysis of tensile decohesion along an interface. J Mech Phys Solids 1990;38:289-324.

[8] Tvergaard V. Effect of fibre debonding in a whisker-reinforced metal. Mater Sci Engng 1990;A125:203-213.

[9] Tvergaard V, Hutchinson JW. The influence of plasticity on mixed mode interface toughness. J Mech Phys Solids 1993;41:1119-1135.

[10] Xu XP, Needleman A. Numerical simulations of fast crack growth in brittle solids. J Mech Phys Solids 1994;42:1397-1434.

[11] Schellekens JCJ, de Borst R. On the numerical integration of interface elements. Int J Numer Meth Engng 1993;36:43-66.

[12] Alfano G, Crisfield MA. Finite element interface models for the delamination analysis of laminated composites: mechanical and computational issues. Int J Numer Meth Engng 2001;50:1701-1736.

[13] de Borst R. Numerical aspects of cohesive-zone models. Engng Fract Mech 2003;70:1743-1757.

[14] de Borst R, Remmers JJC, Needleman A. Mesh-independent discrete numerical representations of cohesive-zone models. Engng Fract Mech 2006;73:160-177.

[15] Turon A, Dàvila CG, Camanho PP, Costa J. An engineering solution for mesh size effects in the simulation of delamination using cohesive zone models. Engng Fract Mech 2007;74:1665-1682.

[16] Harper PW, Hallett SR. Cohesive zone length in numerical simulations in composite delamination. Engng Fract Mech 2008;75:4774-4792.

[17] Park K, Paulino GH. Computational implementation of the PPR potential-based cohesive model in ABAQUS: Educational perpective. Engng Fract Mech 2012;93:239-262.

[18] Reinoso J, Paggi M. A consistent interface element formulation for geometrical and material nonlinearities. Comput Mech 2014;54:1569-1581.

[19] Paggi M, Reinoso J. An anisotropic large displacement cohesive zone model for fibrillar and crazing interfaces. Int J Solids Struct 2015;69-70:106-120.

[20] Ortiz M, Pandolfi A. Finite-deformation irreversible cohesive elements for three-dimensional crack-propagation analysis. Int J Numer Meth Engng 1999;44:1267-1282.

[21] Spring DW, Paulino GH. A growing library of three-dimensional cohesive elements for use in ABAQUS. Engng Fract Mech 2014;126:190-216.

[22] Camanho PP, Dávila CG, De Moura MF. Numerical simulation of mixed-mode progressive delamination in composite materials. J Composite Mater 2003; 37:1415-1438.

[23] Geymonat G, Krasucki F, Lenci S. Mathematical analysis of bonded joint with a soft thin adhesive. Math Mech Solids 1999;4:201-225.

[24] Abaqus. Version 6.9. Dassault Systèmes Simulia Corp.; 2009.

[25] Park K, Paulino GH, Roesler JR. A unified potential-based cohesive model of mixed-mode fracture. J Mech Phys Solids 2009;57:891-908.

[26] Anderson GP, DeVries KL, Williams ML. The peel test in experimental adhesive-fracture mechanics. Exper Mech 1976;16:11-15

[27] Lindley PB. Ozone attack at rubber-metal bond. J Inst Rubber Indus 1971;5:243-248.

[28] Kendall K. The adhesion and surface energy of elastic solids. J Phys D: Appl Phys 1971;4:1186-1195.

[29] Hata T, Gamo M, Doi Y. Mechanics of peeling: Peel equation considering the work of elongation of films and its experimental examination. Kobunshi Kagaku 1965;22:152-159.

[30] Rivlin RS. The effective work of adhesion. Paint Technol 1944;9:1-4.

[31] Kinloch AJ, Lau CC, Williams JG. The peeling of flexible laminates. Int J Fract 1994;66:45-70.

[32] Wei Y, Hutchinson JW. Interface strength, work and adhesion and plasticity in the peel test. Int J Fract 1998;93:315-333.

[33] Rahulkumar P, Jagota A, Bennison SJ, Saigal S. Cohesive element modeling of viscoelastic fracture: application to peel testing of polymers. Int J Solids Struct 2000;37:1873-1897.